Numerical Study on Sinusoidal Fluctuated Pulsatile Laminar Flow Through Various Constrictions

T. S. Lee*, X. Liu, G. C. Li and H. T. Low

Department of Mechanical Engineering, National University of Singapore, Singapore 119260.

Abstract. Numerical simulations have been carried out for laminar sinusoidal pulsating flow in a tube with smooth single constriction. A second-order finite volume method has been developed to solve the fluid flow governing equations on a non-staggered non-orthogonal grid. The effects of the Reynolds number, the Womersley number, the pulsatile amplitude, the constriction ratio and the constriction length on fluid flow in constricted tube will be investigated. It will be demonstrated that the dynamic nature of the pulsating flow greatly depends on the frequency of the flow changes. It is observed that the peak wall vorticity seems to increase with the increase of Reynolds number, the pulsating amplitude and the constriction ratio. The peak values of instantaneous wall vorticity are not greatly affected by the variation of Womersly number. The constriction length does not put a significant impact on the flow instantaneous streamline behaviors compared with other parameters. However, the peak wall vorticity increases monotonically with the decrease of the constriction length.

PACS: 47.11.Df, 47.15.-x, 47.27.nf, 47.50.Cd, 47.63.Cb

Key words: Numerical modeling, constriction, tube, pulsatile flow, control volume.

1 Introduction

The problem of fluid motion in a given domain whose boundaries do not only consist of solid impermeable parts but also include the inflow and outflow parts we will call the 'flowing-through' problem (Moshkin and Mounnamprang, [24]). This problem is

---

*Corresponding author. *Email addresses:* `mpeleets@nus.edu.sg` (T. S. Lee), `liuxi@nus.edu.sg` (X. Liu), `ligengcai@alumni.nus.edu.sg` (G. C. Li), `mpelowht@nus.edu.sg` (H. T. Low)

rather interesting for its applications, especially the flows inside constricted tubes are encountered in many engineering situations, for example fluid flow in pipes with fittings (Lee *et al.* [16]), fluid flow in heat exchangers (Suzuki *et al.* [32]), blood flow in arterial stenoses (Kleinstreuer, [14]), etc.

The research and engineering application of pulsatile fluid flows have been established as a major branch of fluid dynamics. The research on pulsatile flow includes wind energy conversion systems (Azoury, [1]), liquid and solid bulk transportation (Masry and Shobaky, [21]) and biomedical flow phenomena (Tucker, [34]). The principle of pulsatile laminar flow has been applied to practical heat transfer devices, since heat transfer can be enhanced at the incipience of flow instability (Niceno and Nonile, [26]). In biomedical engineering, the pulsatile flow has attracted more and more attention in the investigation of intracardiac flow (Nichols and O'Rourke, 1997 [27]) and blood vessel stenosis flow in recent years as mentioned in Ku [15] and Berger and Jou [2].

It is possible to simulate the flows in a constricted tube by the numerical solution of the unsteady Navier-Stokes equations (Tannehill *et al.* [33], Wesseling [36]). A considerable number of numerical algorithms have been developed for the solution of this equation. Although a large number of investigations has led to better understanding of the flow disturbances induced by a constriction or multiple constrictions, most of the theoretical, numerical and experimental studies have been performed under different simplifying assumptions; for example, the liquid is homogeneous and its viscosity is the same at all rates of shear, it behaves as a Newtonian liquid, the liquid does not slip at the wall, the flow is cylindrical in shape and is rigid.

Berger and Jou [2] reviewed the modeling studies and experiments on steady and unsteady, two- and three- dimensional flows in arteries, and in arterial geometries most relevant in the context of atherosclerosis. They also discussed the work that elucidated many of the pathways by which mechanical forces, primarily the wall shear stresses, were transduced to effect changes in the arterial wall at the cellular, subcellular and genetic level. Mittal *et al.* [22, 23] applied the technique of large-eddy simulation (LES) to the study of pulsatile flow through a modeled arterial stenosis. The inlet volume flux was varied sinusoidally in time in a manner similar to the laminar flow simulations of Tutty [35]. LES was used to compute flow at a peak Reynolds number of 2000 and a Strouhal number of 0.024. Liu and Yamaguchi [18] numerically studied the pulsatile influence on vortical fluid dynamics in the terms of waveform dependence on physiological pulsation with a two-dimensional model of unsteady flow in a stenosed channel. Bertolotti *et al.* [3] simulated three-dimensional unsteady flows through coronary bypass anastomosis by means of both experimental and finite element methods. The host artery included a stenosis shape located at two different distances of grafting. Mahapatra *et al.* [19] numerically solved unsteady Navier-Stokes equations by finite-difference technique in staggered grid distribution for a flow through a channel with locally symmetric and asymmetric constrictions. For flow through symmetric constriction the centerline vertical velocity exhibited finite oscillation behind the constriction at high Reynolds number. Mallinger and Drikakis [20] presented a computational investigation of instabilities

in pulsatile flow through a three-dimensional stenosis. The instability was manifested by asymmetric flow patterns, though the stenosis is axisymmetric, large flow variations in the cross-sectional planes, and swirling motion in the poststenotic region. Liao *et al.* [17] studied numerically the physiological turbulent flow fields in the neighborhoods stenosed arteries for Reynolds numbers from 1000 to 4000. The dimensionless diameter constriction ratios were allowed to vary from 0.375 to 0.6 for bell-shaped constrictions. The Womersley numbers are varied from 6 to 50. The stenosed tube was translated into a rectangular solution domain in a curvilinear co-ordinate system. The solution procedure was based on the method of artificial compressibility with implicit LU-SGS and used a decoupled approach to solve the Reynolds-averaged Navier-Stokes equations and *k-ω* turbulence model equations. The comparison of the numerical solutions to three types of pulsatile flows, including a physiological flow, an equivalent pulsatile flow and a simple pulsatile flow, are made. The comparison of the three pulsatile flows showed that the flow characteristics cannot be properly estimated if an equivalent or simple pulsatile inflow is used instead of actual physiological one in the study of the pulsatile flows through arterial stenosis.

Although numerous investigators have contributed to the understanding of steady and pulsatile flows in a rigid pipe with a constriction, the knowledge in this area is still far from complete. There are a few works on the laminar pulsatile flows, especially on comparison of different types of pulsating flow through various smoothly curved constrictions.

Based on those understandings, the main objectives of the present work are to study numerically different type of laminar pulsatile flow in a pipe with a smoothly curved constriction and investigate the effects of the Womersley number, the Reynolds number, the pulsating amplitude, the constriction ratio and the constriction length on the flow property.

In the present study, the liquid is assumed to be homogeneous, and its viscosity is the same at all rates of shear. The flow behaves as a Newtonian liquid, does not slip at the wall and is laminar. The tube is long compared to the region being studied and is cylindrical in shape. The cross-section of the tube is circular, and the wall of the tube is parallel and rigid. The tube is considered to be straight.

2   Governing equations and numerical procedure

2.1   Governing equations

For axisymmetric flow of incompressible and Newtonian fluids with constant fluid properties, the continuity and Navier-Stokes equations in two-dimensional cylindrical co-ordinates (r,z) can be written in differential conservation form as follows (Bird *et al.*, [4]).
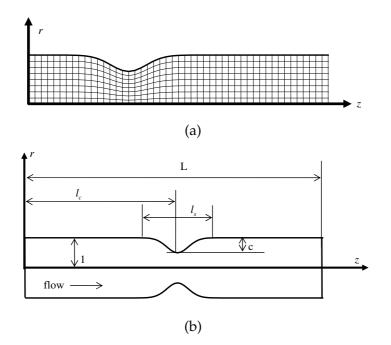
(a)

(b)

Figure 1: Geometric configuration of the constriction (a) Physical solution domain and computational solution domain (b) Dimensionless geometric configuration.

Continuity equation:

$$\frac{1}{r}\frac{\partial(rv_r)}{\partial r}+\frac{\partial v_z}{\partial z}=0; \tag{2.1}$$

r-direction momentum equation:

$$\frac{\partial v_r}{\partial t}+v_r\frac{\partial v_r}{\partial r}+v_z\frac{\partial v_r}{\partial z}=-\frac{1}{\rho}\frac{\partial p}{\partial r}+\frac{\mu}{\rho}\left[\frac{\partial}{\partial r}\left(\frac{1}{r}\frac{\partial(rv_r)}{\partial r}+\frac{\partial^2 v_r}{\partial z^2}\right)\right]; \tag{2.2}$$

z-direction momentum equation:

$$\frac{\partial v_z}{\partial t}+v_r\frac{\partial v_z}{\partial r}+v_z\frac{\partial v_z}{\partial z}=-\frac{1}{\rho}\frac{\partial p}{\partial z}+\frac{\mu}{\rho}\left[\frac{1}{r}\frac{\partial}{\partial r}\left(r\frac{\partial v_z}{\partial r}+\frac{\partial^2 v_z}{\partial z^2}\right)\right]. \tag{2.3}$$

Here, r and z are the physical co-ordinates with the z-axis located along the axis of symmetry of the tube. Fig. 1(a) shows the physical solution domain and computational solution domain of flow through typical constricted tube. No secondary or swirling flows have been allowed so that the total velocity is defined by v_r and v_z, the radial and axial components. The pressure, density and dynamic viscosity are denoted by p, ρ and μ, respectively.

Experimental studies of flows are often carried out on models, and the results are displayed in dimensionless form, thus allowing scaling to real flow conditions. The same

approach can be undertaken in numerical studies as well. The governing equations can be transformed to dimensionless form by using appropriate normalization.

For unsteady pulsatile flow, taking the tube radius (a_0), the mean velocity at inlet (v_0) and the time period of the pulsatile flow (t_0) as the characteristic length, velocity and time respectively, the following non-dimensional variables are defined:

$$r^* = \frac{r}{a_0}, \quad z^* = \frac{z}{a_0}, \quad v_r^* = \frac{v_r}{v_0}, \quad v_z^* = \frac{v_z}{v_0}, \quad t^* = \frac{t}{t_0}, \quad p^* = \frac{p}{\rho v_0^2}. \tag{2.4}$$

If the fluid properties are constant, the dimensionless continuity and Navier-Stokes equations become, omitting the asterisk (*) for simplicity,

$$\frac{1}{r}\frac{\partial(rv_r)}{\partial r} + \frac{\partial v_z}{\partial z} = 0, \tag{2.5}$$

$$St\frac{\partial v_r}{\partial t} + v_r\frac{\partial v_r}{\partial r} + v_z\frac{\partial v_r}{\partial z} = -\frac{\partial p}{\partial r} + \frac{1}{Re}\left[\frac{\partial}{\partial r}\left(\frac{1}{r}\frac{\partial(rv_r)}{\partial r}\right) + \frac{\partial^2 v_r}{\partial z^2}\right], \tag{2.6}$$

$$St\frac{\partial v_z}{\partial t} + v_r\frac{\partial v_z}{\partial r} + v_z\frac{\partial v_z}{\partial z} = -\frac{\partial p}{\partial z} + \frac{1}{Re}\left[\frac{1}{r}\frac{\partial}{\partial r}\left(r\frac{\partial v_z}{\partial r}\right) + \frac{\partial^2 v_z}{\partial z^2}\right], \tag{2.7}$$

where the Reynolds number and the Strouhal number are defined as

$$Re = \frac{\rho v_0 a_0}{\mu}, \tag{2.8}$$

$$St = \frac{a_0}{v_0 t_0}. \tag{2.9}$$

The Womersley number is an indication of the main frequency of the pulsatile flow. It is related to the Reynolds number and the Strouhal number

$$Wo = \sqrt{2\pi \cdot Re \cdot St}. \tag{2.10}$$

2.2 Numerical procedure

The finite volume method is used to discretize the governing equation on a non-staggered non-orthogonal grid. The advantage of the boundary-fitted non-orthogonal grids is that they can be adapted to any geometry, and that optimum properties are easier to achieve than with orthogonal curvilinear grids. Since the grid lines follow the boundaries, the boundary conditions are more easily implemented than with stepwise approximation of curved boundaries (Ferziger and Perić, [8]). The standard algorithm is used with the second-order accuracy of the midpoint rule integral approximation, which is developed and presented below.

The continuity (2.1) and the Navier-Stokes equations (2.2) and (2.3) can be treated partly as scalar equations, and are integrated over a finite number of small control vol-

umes (CV) by applying the Gauss's divergence theorem,

$$\int_S (v_z\mathbf{i}+v_r\mathbf{j})\cdot\mathbf{n}dS=0, \tag{2.11}$$

$$\frac{\partial}{\partial t}\int_\Omega \rho v_r d\Omega + \int_S \rho v_r(v_z\mathbf{i}+v_r\mathbf{j})\cdot\mathbf{n}dS$$
$$=-\int_\Omega \frac{\partial p}{\partial r}d\Omega + \int_S \mu\left(\frac{\partial v_r}{\partial z}\mathbf{i}+\frac{\partial v_r}{\partial z}\mathbf{j}\right)\cdot\mathbf{n}dS - \int_\Omega \mu\frac{v_r}{r^2}d\Omega, \tag{2.12}$$

$$\frac{\partial}{\partial t}\int_\Omega \rho v_z d\Omega + \int_S \rho v_z(v_z\mathbf{i}+v_r\mathbf{j})\cdot\mathbf{n}dS$$
$$=-\int_\Omega \frac{\partial p}{\partial z}d\Omega + \int_S \mu\left(\frac{\partial v_z}{\partial z}\mathbf{i}+\frac{\partial v_z}{\partial z}\mathbf{j}\right)\cdot\mathbf{n}dS, \tag{2.13}$$

where Ω is the closed control volume that is bounded by the surface S, $\mathbf{n}$ is the unit vector orthogonal to S pointing outward from Ω, $\mathbf{i}$, $\mathbf{j}$ are the unit vectors along the z- and r-direction, respectively.

The midpoint rule approximation of the surface and volume integrals is used. The derivative $\partial/\partial z$, $\partial/\partial r$ is calculated using Gauss's divergence theorem.

The mean value of the transported variable at the CV face e is the value at the centre of the cell face. It is expressed in terms of the nodal values and its gradient by employing the central differencing scheme (CDS), which implies linear interpolation between nodes E and C:

$$\phi_e = \frac{z_{ie}-z_C}{z_E-z_C}\phi_E + \frac{z_E-z_{ie}}{z_E-z_C}\phi_C + (z_e-z_{ie})\left(\frac{\partial\phi}{\partial z}\right)_{ie} + (r_e-r_{ie})\left(\frac{\partial\phi}{\partial r}\right)_{ie}$$
$$\left(\frac{\partial\phi}{\partial z}\right)_{ie} = \frac{z_{ie}-z_C}{z_E-z_C}\left(\frac{\partial\phi}{\partial z}\right)_E + \frac{z_E-z_{ie}}{z_E-z_C}\left(\frac{\partial\phi}{\partial z}\right)_C. \tag{2.14}$$

Here, ϕ is a scalar quantity to represent v_z, v_r and p, the node ie lies at the intersection of the cell face and the straight lines connecting nodes C and E.

With these definitions the expression for the mass flux becomes

$$\dot{m}_e = \int_{S_e} \rho(v_z\mathbf{i}+v_r\mathbf{j})\cdot\mathbf{n}dS \approx \rho(S_z^e v_z^e + S_r^e v_r^e). \tag{2.15}$$

The convective flux F^c is evaluated by assuming that the mass flux is known,

$$F_{re}^c = \int_{S^e} \rho v_r(v_z\mathbf{i}+v_r\mathbf{j})\cdot\mathbf{n}dS \approx \dot{m}_e v_r^e,$$
$$F_{ze}^c = \int_{S^e} \rho v_z(v_z\mathbf{i}+v_r\mathbf{j})\cdot\mathbf{n}dS \approx \dot{m}_e v_z^e. \tag{2.16}$$

The diffusion flux F^d involves an estimate of the gradient of v_z and v_r at the CV face,

$$F^d_{re} = \int_{S^e} \mu \left(\frac{\partial v_r}{\partial z} \mathbf{i} + \frac{\partial v_r}{\partial r} \mathbf{j} \right) \cdot \mathbf{n} dS = \mu \left[\left(\frac{\partial v_r}{\partial z} \right)_e S^e_z + \left(\frac{\partial v_r}{\partial r} \right)_e S^e_r \right],$$

$$F^d_{ze} = \int_{S} \mu \left(\frac{\partial v_z}{\partial z} \mathbf{i} + \frac{\partial v_z}{\partial r} \mathbf{j} \right) \cdot \mathbf{n} dS = \mu \left[\left(\frac{\partial v_z}{\partial z} \right)_e S^e_z + \left(\frac{\partial v_z}{\partial r} \right)_e S^e_r \right]. \tag{2.17}$$

The gradient of the variable at the cell face centre is calculated with second-order approximations by using values at auxiliary nodes C' and E', which lie at the intersection of the straight line through cell face centre parallel to the line CE and the straight lines connecting the nodes C and N or E and NE, respectively.

$$\left(\frac{\partial \phi}{\partial z} \right)_e = \frac{(z_e - z_{C'})}{z_{E'} - z_{C'}} \left(\frac{z_{C'} - z_C}{z_N - z_C} \left(\frac{\partial \phi}{\partial z} \right)_N + \frac{z_N - z_{C'}}{z_N - z_C} \left(\frac{\partial \phi}{\partial z} \right)_C \right)$$
$$+ \frac{(z_{E'} - z_e)}{z_{E'} - z_{C'}} \left(\frac{z_{E'} - z_E}{z_{NE} - z_E} \left(\frac{\partial \phi}{\partial z} \right)_{NE} + \frac{z_{NE} - z_{E'}}{z_{NE} - z_E} \left(\frac{\partial \phi}{\partial z} \right)_E \right). \tag{2.18}$$

The midpoint rule approximates a volume integral by the product of the CV centre value of the integrand and the CV volume.

After rearrangement, equations (2.12), (2.13) and (2.11) can be rewritten as algebraic equations of the form

$$A^C_{v_r} v^C_r + A^E_{v_r} v^E_r + A^W_{v_r} v^W_r + A^S_{v_r} v^S_r + A^N_{v_r} v^N_r = Q^C_{v_r},$$
$$A^C_{v_z} v^C_z + A^E_{v_z} v^E_z + A^W_{v_z} v^W_z + A^S_{v_z} v^S_z + A^N_{v_z} v^N_z = Q^C_{v_z}, \tag{2.19}$$
$$A^C_p p^C + A^E_p p^E + A^W_p p^W + A^S_p p^S + A^N_p p^N = Q^C_p,$$

where A is the coefficient, Q is the source that contains all the terms which do not contain unknown variable values. For the solution domain as a whole, the strongly implicit procedure (SIP) method (Stone, 1968) [31] is used for the resulting matrix equations:

$$[A_{v_r}]\{v_r\} = \{Q_{v_r}\}, \quad [A_{v_z}]\{v_z\} = \{Q_{v_z}\}, \quad [A_p]\{p\} = \{Q_p\}. \tag{2.20}$$

The coupled series equations for v_z, v_r and p are solved by the SIMPLE algorithm (Pantankar, [28]). The numerical procedure can be briefly outlined as follows.

1) The steady flow is computed and taken as initial condition for the unsteady flow computation. Start calculation of the fields at the new time using the previous iteration values for pressure, mass fluxes and other variables.

2) The v_z and v_r matrix equations in (2.20) are solved by applying the SIP algorithm. The residual of the continuity equation is computed with the new mass fluxes based on the just calculated velocity field and used as the source term of the pressure correction equation (p matrix equation in (2.20)), which is solved by using SIP until the residuals are reduced to 0.1 of their values at the first iteration. The mass fluxes,

velocity components and pressure are then corrected with the calculated pressure correction. Repeat this step until convergence. The convergence criterion is that the sum of absolute residuals in all equations is reduced by four orders of magnitude (0.01%).

3) At convergence the stream function and the vorticity field are computed from the velocity field. Information about the pressure is obtained from the pressure field.

4) Advance to the next time step.

5) Advance to the next time cycle

2.3   Geometrical model

The geometrical model used in the present study is a two-dimensional axisymmetrical smooth shape constriction in a rigid tube (Fig. 1(b)). It is specified as the symmetric cosine curve (Deshpande *et al.* [6], Young and Tsai [37], Fukushima *et al.* [9], Siegel *et al.* [30], Zendehbudi and Moayeri [38]). The equation used to generate the geometry of the model is of the form

$$
\begin{aligned}
R(z) &= 1 - \frac{c}{2}\left[1 + \cos\left(2\pi\frac{z - l_c}{l_c}\right)\right] && \text{if } |(z - l_c)| \le \frac{l_s}{2}; \quad 0 \le z \le L, \\
R(z) &= 1 && \text{if } |(z - l_c)| \ge \frac{l_s}{2}; \quad 0 \le z \le L,
\end{aligned}
\tag{2.21}
$$

where c is the dimensionless constriction ratio, l_c is the dimensionless distance to the centre of constriction from the inlet of tube, l_s is the dimensionless length of the constriction, and L is the total length of the tube.

3   Validation of computational results

To evaluate the present numerical procedure and check the validity of the numerical result, the following test cases are considered:

3.1   Steady flow through the cosine curve constricted tube

The pertinent geometrical characteristics of this model is summarized as that the dimensionless constriction ratio c is 0.667, the dimensionless distance to the centre of constriction from the inlet of tube l_c is 16, the dimensionless length of the constriction l_s is 4, and the total length of the tube L is 32 (2.21). This model duplicates the Model M3 investigated numerically by Deshpande *et al.* [6] and is employed experimentally by Young and Tsai [37], so that comparisons can be made with previous numerical and experimental results to check the validity of the numerical results.

The present numerical predictions of the separation and reattachment points are compared with the experimental data and other numerical solutions. The locations of separation points agree favorably. A greater disagreement is found for the reattachment point.

This is not surprising since the reattachment points are difficult to ascertain experimentally. The difference between numerical simulations is possible because of the way the outlet boundary condition formulated. Deshpande *et al.* [6] assumed Poiseulle flow at infinite distance downstream of constriction, while the present study assumes an unrestrictive flow at the outlet and allows the flow profile to develop on its own. However, the two results share a common validity. The onset of separation was observed experimentally to occur at a Reynolds number of 10 (Young and Tsai, [37]), numerically at a value of 8.75 by Deshpande *et al.* [6], and 8.7 by our calculations. The present study gives separation more downstream than Deshpande *et al.* [6] did, and predicts a reattachment point more upstream than Deshpande *et al.* [6] did.

We define the pressure drop Δp_z over a tube length z by

$$\Delta p_z = \int_0^z -\frac{\partial p}{\partial z} dz. \tag{3.1}$$

The comparison of the dimensionless pressure drop is made with Deshpande *et al.* [6]. The agreement here is rather good.

The wall vorticity is related to the tube wall shearing stress in Newtonian flows. Since there is no reliable method of determining the wall shear stress experimentally, the theoretical calculations offer some insight to the behavior of the quantity. The variation of the maximum wall vorticity and the Reynolds number is compared with the data of Deshpande *et al.* [6]. The results are presented by a similar curve. The difference is obvious due to the way the outlet boundary condition is formulated. Where the two results share a common validity, however, the agreement is quite good.

3.2 Unsteady entrance flow development in a straight tube

To investigate the accuracy and computational efficiency of the present method, the sinusoidal fluctuated pulsatile laminar flow in a short tube without constrictions is carried out by comparing their predictions with the results obtained by other researchers in the developing region of the entrance laminar flow in a straight tube. The dimensionless radius and the dimensionless length of the tube were taken as 1 and 50 respectively. The Womersley number and the Reynolds number were taken as 12.5 and 100, respectively. The dimensionless velocities at the inflow boundary were specified by

$$v_{z\text{in}} = 1 + \sin\left(2\pi\frac{t}{T}\right), \quad v_{r\text{in}} = 0. \tag{3.2}$$

A blunt entrance profile was used for the upstream flow which varied in a sinusoidal fashion, and the initial values of the variables in the computational field were set to zero except boundary.

Calculations were carried out for a uniform grid size of 250 and 40 nodes along the radial and axial directions respectively, and the time step in each cycle of 80, which a gives grid independent solution for present method.

The pulsatile flows were computed over sufficiently long time to obtain a periodic solution, namely a solution that did not change measurably from one cycle to the next. To avoid any chance for transient effects, all results correspond to ten cycles.

In order to verify the accuracy of the computational results for unsteady flow, the axial velocity profile far downstream was compared with He *et al.* (1994) [11] at phases 90 degree and 270 degree. Excellent agreement was observed.

The comparisons between the downstream axial velocity profile of the sinusoidal fluc-tuated flow with sinusoidal flow at four certain time steps (phase 0, 90, 180 and 270 degree) and steady flow profile are shown in Fig. 3. The axial velocity profiles of the si-nusoidal fluctuated flow and sinusoidal flow are significantly different from a parabolic velocity profile (Poiseuillean). It can be seen clearly that the velocity profile of the sinu-soidal fluctuated flow was obtained when we added the velocity profile of pure sinu-soidal flow to the velocity profile of the steady flow.

The comparisons between the current numerical results and the experimental data and others numerical solutions show that the current numerical solvers are capable of simulating laminar flow in the constricted tube with good accuracy and stability.

4   Result and discussion

In this section, the numerical procedure described in Section 2 is applied to the pulsat-ing flow simulations. Different types of sinusoidal fluctuated pulsatile laminar flow in a tube with cosine curved smooth axisymmetric single constriction are then comparatively studied to investigate the effect of the Womersley number, the Reynolds number and the pulsating amplitude. The pulsating flow through various cosine curved smooth axisym-metric single constrictions is also studied to investigate the effects of the constriction ratio and the constriction length.

4.1   Geometrical configuration

The pertinent geometrical characteristics of this model is summarized as that the dimen-sionless constriction ratio c varies from 1/3 to 2/3, the dimensionless length of the con-striction l_s is adjusted from 1 to 4, the dimensionless length of the entrance region (l_c-l_s) is 10 and the total length of the tube L varies from 41 to 44 (2.21).

4.2   Pulsating flow configuration and boundary conditions

For pulsating inlet flow, the flow rate Q is specified as uniform steady flow with an im-posed sinusoidal fluctuation,

$$Q = Q_m \left[1 + A \sin \left(2\pi \frac{t}{T} \right) \right], \tag{4.1}$$
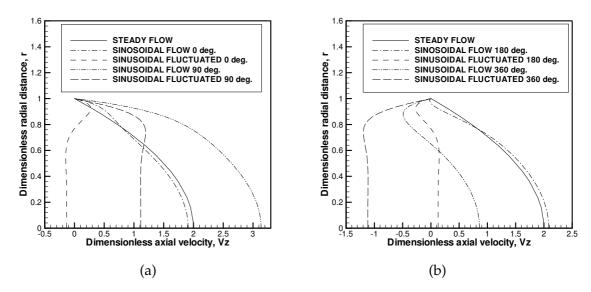
Figure 2: Comparison of inflow axial velocity profiles of sinusoidal fluctuated flow with sinusoidal flow and steady flow profiles (a) phases 0 and 90 degree (b) phases 180 and 270 degree.
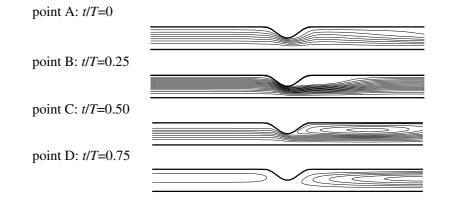

Figure 3: Instantaneous streamlines for sinusoidal fluctuated flow when Re$=100$, Wo$=12.5$, $A=1$, $C=0.5$, $ls=2$.

where Q is the flow rate, Q_m is the mean flow rate, T is the time period of the pulsation t is time and A is the pulsating amplitude. This type of flow is often used in the initial studies for pulsatile blood flows and many other engineering applications, e.g. Huang *et al.* [13], Lee *et al.* [16], Deplano and Siouffi [7].

The inlet velocity profiles at each time step are significantly different from a parabolic velocity profile (Poiseuillean) for the Womersley numbers greater than about one (Gary, [10]). It can be carried out by hand with tables, using a simple computer program in Mathematica (He *et al.* [11]) or by Fourier analysis (Rosenfeld [29]), Daily and Pletcher [5], Neofytou and Drikakis [25]. In the current study the profile corresponding to pulsat-

ing laminar fully developed entrance flow in a straight tube is employed as the inflow condition. A laminar inflow condition is appropriate for the Womersley number, the Strouhal number and the Reynolds number employed in the current study. The down-stream outlet boundary conditions are specified with fully developed flow. The outflow is considered as fully developed. Along a solid wall, the non-slip condition is assured, that is, all velocity components are equal to zero on the wall. Along the centerline, the axisymmetric condition is applied for all variables.

The Womersley numbers from 1 to 12.5, which are physiologically relevant for most medium to small arteries (Tutty [35], Huang *et al.* [13], Ku [15]), are considered here, with the Reynolds number varying from 20 to 200. The pulsating amplitude A varies from 0 to 2, where $A=0$ corresponds to the steady flow.

In this study, the results are compared by considering some selected points, including four points corresponding to the conditions of mean accelerated, before peak, mean decelerated and after peak flow rates on each waveform. The phases of these points are 0, 90, 180 and 270 degree, corresponding to the time of $0T$, $0.25T$, $0.5T$ and $0.75T$, respectively.

4.3   Basic case: $\mathbf{Re}=100$, $\mathbf{Wo}=12.5$, $A=1$, $C=0.5$, $ls=2$

The sinusoidal fluctuated flow with Re$=100$, Wo$=12.5$, $A=1$ for a moderate constriction $C=0.5$, $ls=2$ will be taken as a 'basic case' for a number of comparisons.

For arterial application, the interest is in the time-dependent flow fields. The instantaneous streamlines of the sinusoidal fluctuated flow show considerable variation throughout the cycle (Fig. 3). At point A, $t/T=0$, where the instantaneous Reynolds number is equal to the mean one in the accelerated flow of the total flux, the streamlines are different from those in the steady flow. The streamlines run smoothly through the constriction flow field with a small vortex nestled in the concavity of the constriction contour, the separation and reattachment points are located close to the inflection point of the wall curve. As the flow accelerates to the peak flow rate point B, where $t/T=0.25$, the attached vortex grows longer and fatter. Past the peak flux, as the flow decelerates, the attached vortex continues to grow in size. At point C, $t/T=0.5$, where the instantaneous Reynolds number equals the mean one during decelerated flow of the total flux, the vortex occupies about 75% of the total distal area. When the flow rate reach its zero net flux and relatively low velocities at point D, $t/T=0.75$, the remnants of these detached vortices occupy most of the constriction flow area, not only the distal to the throat, but also the proximal to the throat. When t/T further advances to 1, the next cycle restarts and the flow follows a repeated pattern.

Although the streamline pictures show more detail, the flow behavior can be shown more clearly by presenting the wall vorticity distribution at different time steps (Fig. 4). The instantaneous wall vorticity varies during the cycle, being higher than the wall vorticity of the steady flows under the same mean Reynolds number in some parts of the cycle, and lower in other parts. The maximum wall vorticity, which also occurs close to
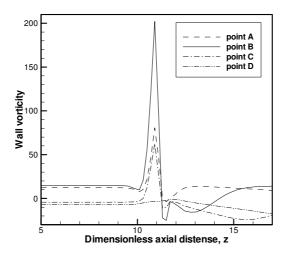
Figure 4: Wall vorticity distribution at different time steps for sinusoidal fluctuated flow when Re=100, Wo=12.5, $A=1$, $C=0.5$, $ls=2$.
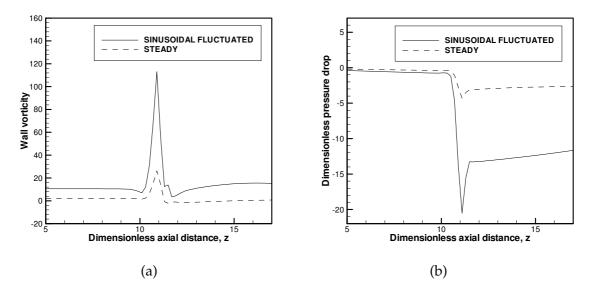

(a)   (b)

Figure 5: Root mean square wall vorticity distribution (a) and time-average pressure drop (b) in one cycle when Re$=100$, Wo$=12.5$, $A=1$, $C=0.5$, $ls=2$

the minimum constriction plane at the peak flow rate point *B*, is higher than the steady flow. The maximum wall vorticity at the points *A* and *C* is also higher than the steady flow, while the instantaneous Reynolds number equals the mean one.

For unsteady flow, the mean wall vorticity, rather than the peak value, is used as the criterion. In order to observe more clearly, the root mean square wall vorticity distributions in one cycle is presented in Fig. 5(a). It can be seen that the maximum mean wall

vorticity is consistently higher than the equivalent steady-state value. The time-average pressure drop at various time steps is shown in Fig. 5(b). It shows that the unsteady flow produces a higher pressure drop than the steady flow.

4.4   The effects of the Reynolds number

It has been know that the Reynolds number has a great influence on the flow field in the constricted tube for a steady flow. The effects of the Reynolds number on the unsteady pulsating flow are discussed in this study. The Reynolds numbers of 20, 100 and 200 are considered here, with the Womersley number being fixed to 12.5, and the constriction ratio and the constriction length being fixed to 2 and 0.5 respectively. The pulsating amplitude A is set to be 1.

The instantaneous streamlines for sinusoidal fluctuated flow at $Re = 20$ and 200 are shown in Figs. 6(a) and 6(b) respectively. Referring to the streamlines in Figs. 3, 6(a) and 6(b), at the point A, $t/T = 0$, for $Re = 20$, the streamlines run smoothly through the constriction flow field. However, for $Re = 200$, there is a bigger vortex in the streamlines nestled in the concavity of the constriction contour compared to the case of $Re = 100$. At the peak flow rate point B, where $t/T = 0.25$, the attached vortex grows longer for $Re = 200$, and becomes shorter for $Re = 20$. Past the peak flux, as the flow decelerates, the attached vortex continues to grow in size. At the point D, $t/T = 0.75$, where the flow rate reaches its zero net flux, the remnants of these detached vortices occupy the distal to the throat as well as the proximal to the throat. However, the shortest vortex is for $Re = 20$. It can be seen that the variation of the Reynolds number can greatly influence the flow pattern.

Since the magnitudes of the peak wall vorticity near the constriction at peak flow rate point B are always higher than the ones at other points, only the comparison of instantaneous wall vorticity distributions at point B is presented in Fig. 7(a) for conciseness. The value of the maximum wall vorticity increases monotonically with the increase of the Reynolds number. The location of the peak wall vorticity tends to shift slightly upstream as the Reynolds number increases. The comparison of the root mean square wall vorticity distributions in one cycle is presented in Fig. 7(b). It can be seen that the maximum mean wall vorticity is consistently higher for higher Reynolds number than the one for low Reynolds number. The increase of the Reynolds number from 100 to 200 causes a 50% increase of the maximum wall vorticity. For $Re = 100$ and 200, the wall vorticity downstream the constriction does not seem to regain its undisturbed upstream values as it does for $Re = 20$. This is due to the increase in size of the recirculation region.

It can be concluded that the flow pattern can be greatly influenced by the variation of the Reynolds number. Higher Reynolds numbers can cause the peak wall vorticity to increase sharply.
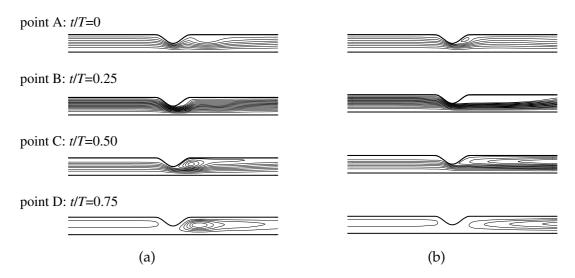
point A: *t/T*=0

point B: *t/T*=0.25

point C: *t/T*=0.50

point D: *t/T*=0.75

(a)   (b)

Figure 6: Instantaneous streamlines for sinusoidal fluctuated flow when Re $=20$ (a) and 200 (b), Wo $=12.5$, $A=1$, $C=0.5$, $ls=2$.

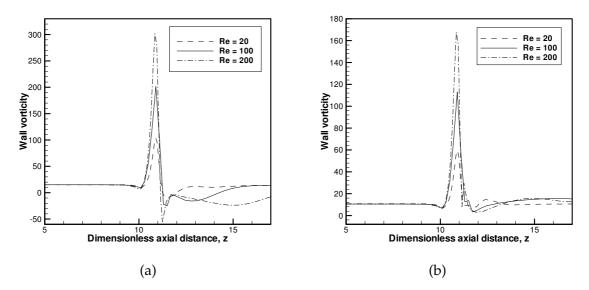(a)   (b)

Figure 7: Comparison of wall vorticity distribution at B (phase 90 degree) (a) and root mean square wall vorticity distribution in one cycle (b) when Re $=20$, 100 and 200.

4.5 The effects of the Womersley number

In order to elucidate the effects of the Womersley number, the details of flow fields for different Womersley numbers are examined without varying the Reynolds number and the shape of the constriction. The Womersley numbers 1, 6 and 12.5 are taken into account

here, with the Reynolds number being fixed to 100, and the constriction ratio and the constriction length being fixed to 2 and 0.5 respectively. The pulsating amplitude A is set to be 1.

The instantaneous streamlines for Wo $=6$ and 1 at the selected time levels are shown in Figs. 8(a) and 8(b) respectively. Referring to the streamlines in Figs. 3, 8(a) and 8(b), the difference in flow patterns can be noticed for different Womersley numbers. For a comparatively low Womersley number, the flow pattern looks similar to those of the quasi-unsteady flow. There is always a recirculating vortex forming downstream the constriction for nonzero instantaneous flow rate for low Womersley number. The flow field is mainly affected by the current instantaneous flow rate for low Womersley numbers. In contrast, the flow field can be strongly influenced by the flow rate at previous time levels for higher Womersley numbers. Since the upstream flow rate predominates in the periodic development of the flow field, the recirculation zone almost always occurs on the downstream side of constriction, except for the instant flow rate being zero or nearly zero. It is interesting that the recirculation zones always prefer to simultaneously occur both the proximal and the distal to the constriction when the instant net flow rate approaches zero for each Womersley number.

The instantaneous wall vorticity distributions at the peak upstream flow rate point B are displayed in Fig. 9(a) for the Womersley numbers 1, 6 and 12.5. It can be seen that the peak values of instantaneous wall vorticity are not greatly affected by the variation of the Womersley number. However, the wall vorticity downstream the constriction for Wo $=12.5$ recovers rapidly to the same level as that of the constriction upstream, while this is not a case for the Womersley numbers 1 and 6.

The comparison of the root mean square wall vorticity distributions in one cycle is presented in Fig. 9(b). It can be seen that the mean wall vorticity distributions are almost the same for the three different Womersley numbers.

The Womersley number can be interpreted as the ratio of unsteady force to viscous force. The dynamic nature of the flow greatly depends on the frequency of the flow. At low Womersley numbers, the difference of flows of different Womersley numbers is less, while high Womersley number puts a significant impact on the flow behaviors. The Womersley number does not greatly affect the maximum and mean wall vorticity distributions.

4.6   The effects of the pulsating amplitude

The details of flow fields for different sinusoidal pulsating amplitude are examined, without varying the Reynolds number, the Womersley number and the shape of the constriction, to investigate the effects of the sinusoidal pulsating amplitude on the developing flow characteristics. The pulsating amplitude A is set to be 0.5, 1 and 2. The Womersley number of 12.5 and the Reynolds number of 100 are considered here with the constriction ratio and the constriction length being fixed to 2 and 0.5, respectively.

The instantaneous streamlines for sinusoidal fluctuated flow at $A = 0.5$ and 2 are
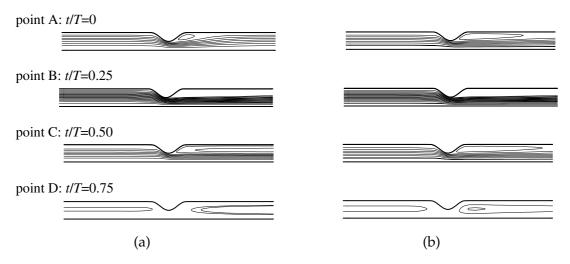
point A: t/T=0

point B: t/T=0.25

point C: t/T=0.50

point D: t/T=0.75

(a)   (b)

Figure 8: Instantaneous streamlines for sinusoidal fluctuated flow when Wo=6 (a) and 1 (b), Re=100, A=1, C=0.5, ls=2.

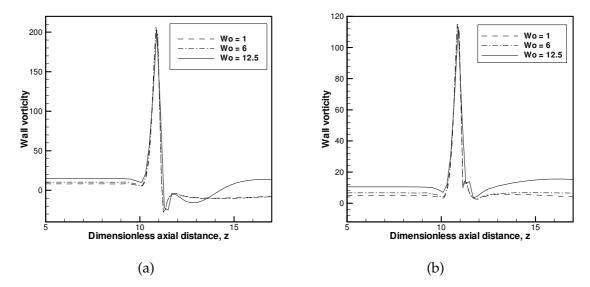(a)   (b)

Figure 9: Comparison of wall vorticity distribution at B (phase 90 degree) (a) and root mean square wall vorticity distribution in one cycle (b) when Wo=1, 6 and 12.5.

shown in Figs. 10(a) and 10(b) respectively. Referring to the streamlines in Figs. 3, 10(a) and 10(b), at point A, $t/T=0$, for $A=2$, the streamlines run smoothly through the constriction flow field with the vortex nestled in the center of the tube at the proximal to the throat. However, for $A=0.5$, there is a bigger vortex nestled in the concavity of the constriction contour compared to the case of $A=1$. As the flow accelerates to the peak flow rate point B, where $t/T=0.25$, the attached vortex grows longer for $A=2$, being

similar for $A = 1$ and 0.5. Past the peak flux, as the flow decelerates, the attached vortex continues to grow in size. Since the flow rate of $A = 2$ is reverse now, the vortex occurs on the left side of the constriction. When the flow rate reaches its minimum value at the point D for $A = 0.5$, $t/T = 0.75$, the remnants of these detached vortices occupy most of the constriction flow area including the distal to the throat. For $A = 2$, remnants of these detached vortices occupy most of the constriction flow area including the proximal to the throat, and the vortex now is separated from the wall.

The comparison of instantaneous wall vorticity distributions at the point B is presented in Fig. 11(a). The value of the maximum wall vorticity increases monotonically with increasing pulsating amplitude because the flow rate is increased. The value of maximum wall vorticity when $A = 2$ is twice as larger as the value when $A = 1$, and three times larger than the value when $A = 0.5$. The comparison of the root mean square wall vorticity distributions in one cycle is presented in Fig. 11(b). It can be seen that the maximum mean wall vorticity is consistently higher for higher pulsating amplitude, and the wall vorticity downstream the constriction for high amplitude does not seem to regain its upstream value as it does for low pulsating amplitude. Larger pulsating amplitude can cause the peak wall vorticity to increase sharply.

4.7   The effects of the constriction ratio

It is obvious that the constriction ratio has a great influence on the flow field in a constricted tube. In this study, we discuss how the characteristics of the flow vary with the variation of the constriction ratios for the pulsating flow. The numerical results are compared for the three different constriction ratios 1/3, 1/2 and 2/3. The Womersley number of 12.5 is considered here, with the Reynolds number being fixed to 100 and the constriction length being fixed to 2. The pulsating amplitude A is fixed to 1.

The instantaneous streamlines for sinusoidal fluctuated flow at $C = 1/3$ and 2/3 are shown in Figs. 12(a) and 12(b) respectively. Referring to the streamlines in Figs. 3, 12(a) and 12(b), at point A, $t/T = 0$, for $C = 1/3$, the streamlines run smoothly through the constriction flow field. However, for $C = 2/3$, there is a bigger vortex nestled in the concavity of the constriction contour compared to the case of $C = 1/2$. At the peak flow rate point B, where $t/T = 0.25$, the attached vortex grows longer for $C = 2/3$ and becomes shorter for $C = 1/3$. The attached vortex continues to grow in size as the flow decelerates. When the flow rate reaches zero net flux at the point D, $t/T = 0.75$, the remnants of these detached vortices occupy both the distal and the proximal to the throat. The shortest vortex is for $C = 1/3$.

The comparison of instantaneous wall vorticity distributions at the point B is presented in Fig. 13(a). The value of the maximum wall vorticity increases monotonically with increasing constriction ratio. The value of the maximum wall vorticity when $C = 2/3$ is 5.5 times larger than the value when $C = 1/3$, and 3 times larger than the value when $C = 1/2$.

The comparison of the root mean square wall vorticity distributions in one cycle is
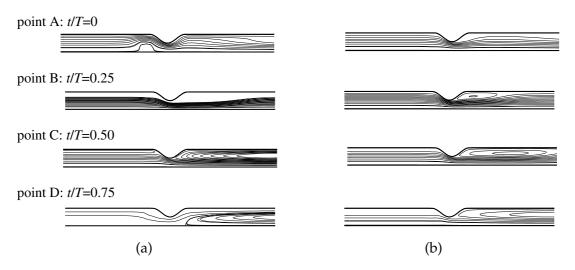
point A: *t/T*=0

point B: *t/T*=0.25

point C: *t/T*=0.50

point D: *t/T*=0.75

(a)   (b)

Figure 10: Instantaneous streamlines for sinusoidal fluctuated flow when $A=2$ (a) and 0.5 (b), $\mathrm{Wo}=12.5$, $\mathrm{Re}=100$, $C=0.5$, $ls=2$.

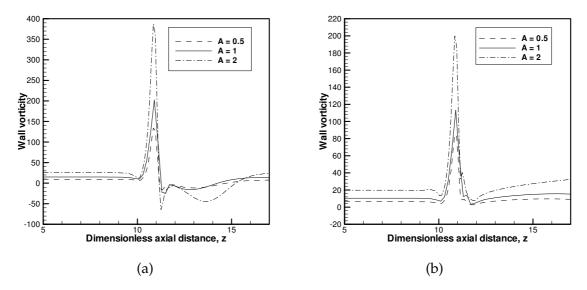(a)   (b)

Figure 11: Comparison of wall vorticity distribution at B (phase 90 degree) (a) and root mean square wall vorticity distribution in one cycle (b) when $A=0.5$, 1 and 2.

presented in Fig. 13(b). It can be seen that for a narrow constriction, the maximum mean wall vorticity is consistently high, and the wall vorticity downstream the constriction seems to regain its upstream value quickly.

It can be concluded that the severe constriction ratio leads to a more complex flow field. The peak wall vorticity tends to increase with increasing constriction ratio.
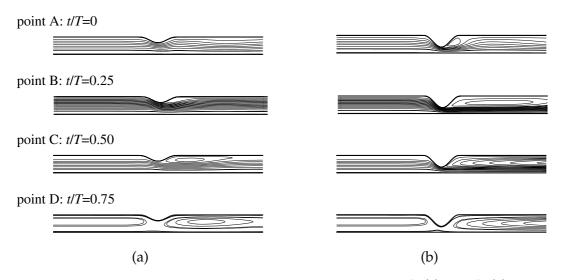
point A: t/T=0

point B: t/T=0.25

point C: t/T=0.50

point D: t/T=0.75

(a)   (b)

Figure 12: Instantaneous streamlines for sinusoidal fluctuated flow when $C=1/3$ (a) and 2/3 (b), Wo$=12.5$, Re$=100$, $A=0.5$, $ls=2$.

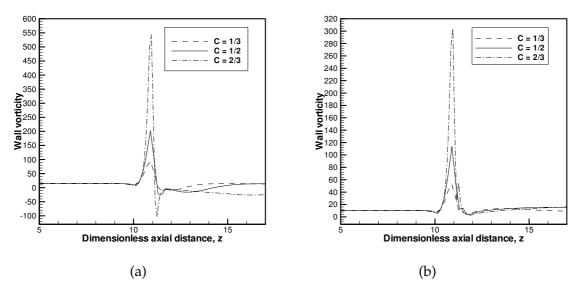(a)   (b)

Figure 13: Comparison of wall vorticity distribution at B (phase 90 degree) (a) and root mean square wall vorticity distribution in one cycle (b) when $C=1/3$, $1/2$ and $2/3$.

4.8   The effects of the constriction length

We now discuss how the characteristics of the flow vary with the variation of constriction length for the pulsating flow. The numerical results are compared for three different constriction lengths, namely 1, 2 and 4. The Womersley number of 12.5 is considered, here with the Reynolds number being fixed to 100 and the constriction ratio being fixed
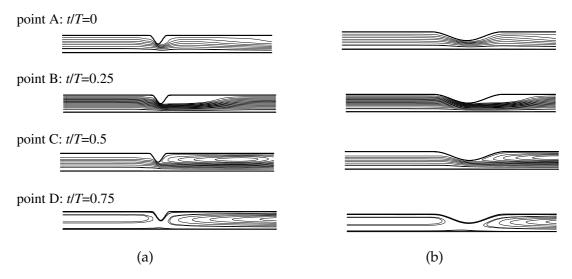
point A: $t/T=0$

point B: $t/T=0.25$

point C: $t/T=0.5$

point D: $t/T=0.75$

(a)   (b)

Figure 14: Instantaneous streamlines for sinusoidal fluctuated flow when $ls=1$ (a) and 4 (b), Wo=12.5, Re=100, $A=0.5$, $C=0.5$.

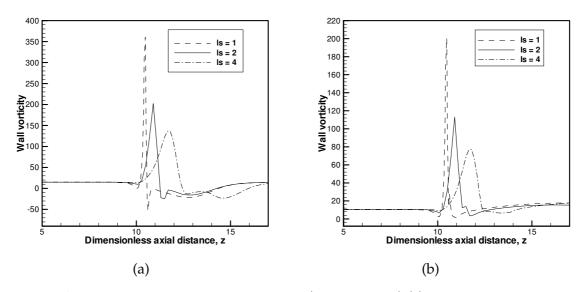(a)   (b)

Figure 15: Comparison of wall vorticity distribution at B (phase 90 degree) (a) and root mean square wall vorticity distribution in one cycle (b) when $ls=1$, 2 and 4.

to $1/2$. The pulsating amplitude A is fixed to 1.

The instantaneous streamlines for sinusoidal fluctuated flow at $ls=1/3$ and $2/3$ are shown in Figs. 14(a) and 14(b), respectively. The instantaneous streamlines are similar for the three cases with regards to the streamlines in Figs. 3, 14(a) and 14(b). Compared to other parameters the constriction length does not have a significant impact on the flow instantaneous streamline behaviors.

The comparison of instantaneous wall vorticity distributions at the point B is presented in Fig. 15(a). The value of the maximum wall vorticity increases monotonically with decreasing constriction length. The value of the maximum wall vorticity when $ls = 1$ is twice as larger as the value when $ls = 2$, and three times larger than the value when $ls = 4$.

The comparison of the root mean square wall vorticity distributions in one cycle is presented in Fig. 15(b). The maximum mean wall vorticity is consistently higher for longer constriction than for shorter constriction. Long constriction tends to decrease the value of peak wall vorticity.

5   Conclusions

A finite volume method has been developed to solve the fluid flow governing equations on a non-staggered non-orthogonal grid. The flow governing equations are expressed in primitive variable form. The SIMPLE algorithm is used to solve these equations, with the variable terms approximated by second-order difference schemes. The SIP algorithm is used in solving the resulting matrix equations. With this numerical method and the boundary-fitted grids, optimum properties are easier to achieve than with orthogonal curvilinear grids, and the boundary conditions are more easily implemented than with stepwise approximation of curved boundaries.

The present numerical method has been evaluated by calculating steady laminar flow through a cosine curve constricted tube and unsteady entrance laminar flow development in a straight tube. Comparisons have been made between its state solutions and the experimental data and other numerical solutions reported in literature. Then it has been applied to the calculation of laminar steady and pulsating flow in a tube with single constriction.

The effects of the Reynolds number, the Womersley number, the pulsatile amplitude, the constriction ratio and the constriction length of fluid flow in constricted tube were investigated by comparing the results of instantaneous streamlines, instantaneous wall vorticity distribution, and root mean square wall vorticity distribution.

From the numerical investigation of the sinusoidal fluctuated flows, the following conclusions can be drawn:

1) The recirculation region and the recirculation points in pulsating flows change in size and location with time, due to the variation of the instantaneous flow rate. There is no constant flow stationary point in the pulsatile flow. The conclusions regarding fluid dynamical effects in unsteady flow cannot be based solely on the mean flow.

2) The variation of the Reynolds numbers can greatly influence the flow pattern. The maximum mean wall vorticity is consistently higher for higher Reynolds numbers than the ones for lower Reynolds numbers.

3) The dynamic nature of the flow greatly depends on the frequency of the flow change. The recirculation zones always prefer to occur simultaneously both the proximal and the distal to the constriction when the instant net flow rate approaches zero for each Womersley number. The peak values of the instantaneous wall vorticity are not greatly affected by the variation of the Womersley number.

4) The flow deceleration in the pulsating cycles tends to enlarge the recirculation region, and this effect becomes more significant with increasing pulsating amplitude. The maximum mean wall vorticity is consistently high for high pulsating amplitude.

5) The maximum mean wall vorticity is consistently high for severe constriction ratio.

6) Compared to other parameters the constriction length does not have a significant impact on the flow instantaneous streamline behavior. Short constriction can cause the peak wall vorticity to increase dramatically.

References

[1] P. H. Azoury, Engineering Applications of Unsteady Fluid Flow, John Wiley & Sons, New York, 1992.

[2] S. A. Berger and L. D. Jou, Flows in stenotic vessels, Annu. Rev. Fluid Mech., 32 (2000), 347-382.

[3] C. Bertolotti, V. Deplano, J. Fuseri and P. Dupouy, Numerical and experimental models of post-operative realistic flows in stenosed coronary bypass, J. Biomech., 34 (2001), 1049-1064.

[4] R. B. Bird, W. E. Stewart and E. N. Lightfoot, Transport Phenomena, J. Wiley, New York, 2002.

[5] L. D. Dailey and R. H. Pletcher, Evaluation of multigrid acceleration for preconditioned time-accurate Navier-Stokes algorithms, Comput. Fluids, 25 (1996), 791-811.

[6] M. D. Deshpande, D. P. Giddens and R. F. Mabon, Steady laminar flow through modelled vascular stenoses, J. Biomech., 9 (1976), 165-174.

[7] V. Deplano and M. Siouffi, Experimental and numerical study of pulsatile flows through stenosis: Wall shear stress analysis J. Biomech., 32 (1999), 1081-1090.

[8] J. H. Ferziger and M. Perić, Computational Methods for Fluid Dynamics, Springer, Berlin, 2001.

[9] T. Fukushima, T. Azuma and T. Matsuzawa, Numerical analysis of blood flow in the vertebral artery, J. Biomech. Eng. ASME, 104 (1982), 143-147.

[10] L. L. Gary, Laminar Flow and Convective Transport Processes, Butterworth-Heinemann, Stoneham, 1992.

[11] X. He, D. N. Ku and J. E. Moore, Simple calculation of the velocity profiles for pulsatile flow in a blood vessel using Mathematica Ann. Biomed. Eng., 21 (1993), 45-49.

[12] X. He and D. N. Ku, Unsteady entrance flow development in a straight tube, J. Biomech. Eng., 116 (1994), 355-360.

[13] H. Huang, V. J. Modi and B. R. Seymour, Fluid mechanics of stenosed arteries, Int. J. Eng. Sci., 33 (1995), 815-828.

[14] C. Kleinstreuer, Engineering Fluid Dynamics, Cambridge University Press, London, 1997.

[15] D. N. Ku, Blood flow in arteries, Annu. Rev. Fluid Mech., 29 (1997), 399-434.

[16] T. S. Lee, T. W. Ng and Z. D. Shi, Numerical study of effects of pulsatile amplitude on unsteady laminar flows in rigid pipe with ring-type constrictions, Int. J. Numer. Meth. Fluids, 24 (1997), 275-290.

[17] W. Liao, T. S. Lee and H. T. Low, Numerical study of physiological turbulent flows through stenosed arteries, Int. J. Mod. Phys. C, 14 (2003), p. 635-659.

[18] H. Liu and T. Yamaguchi, Waveform dependence of pulsatile flow in a stenosed channel, J. Biomech. Eng. ASME, 123 (2001), 88-96.

[19] T. R. Mahapatra, G. C. Layek and M. K. Maiti, Unsteady laminar separated flow through constricted channel, Int. J. Nonlinear Mech., 37 (2002), 171-186.

[20] F. Mallinger and D. Drikakis, Instability in three-dimensional unsteady stenotic flows, Int. J. Heat Fluid Fl., 23 (2002), 657-663.

[21] O. A. Masry and K. Shobaky, Plusating slurry flow in pipeline, Exp. Fluids, 7 (1989), 481-486.

[22] R. Mittal, S. P. Simmons and H. S. Udaykumar, Application of large-eddy aimulation on the study of pulsatile flow in a modeled arterial stenosis, J. Biomech. Eng. ASME, 123 (2001), 325-332.

[23] R. Mittal, S. P. Simmons and F. Najjar, Numerical study of pulsatile flow in a constricted channel, J. Fluid Mech., 485 (2003), 337-378.

[24] N. P. Moshkin and P. Mounnamprang, Numerical simulation of vortical ideal fluid flow through curved channel, Int. J. Numer. Meth. Fluids, 41 (2003), 1173-1189.

[25] P. Neofytou and D. Drikakis, Effects of blood models on flows through a stenosis, Int. J. Numer. Meth. Fluids, 43 (2003), 597-635.

[26] B. Niceno and E. Nonile, Numerical analysis of fluid flow and heat transfer in periodic wavy channels, Int. J. Heat Fluid Fl., 22 (2001), 156-167.

[27] W. W. Nichols and M. F. O'Rourke, McDonald's Blood Flow in Arteries, Arnold, London, 1997.

[28] S. V. Pantankar, Numerical Heat Transfer and Fluid Flow, McGraw-Hill, New York, 1980.

[29] M. Rosenfeld, Validation of numerical simulation of incompressible pulsatile flow in a constricted channel, Comput. Fluids, 22 (1993), 139-156.

[30] J. M. Siegel, C. P. Markou, D. N. Ku and S. R. Hanson, A scaling law for wall shear rate through an arterial stenosis, J. Biomech. Eng. ASME, 116 (1994), 446-451.

[31] H. L. Stone, Iterative solution of implicit approximations of multidimensional partial differential equations, SIAM J. Numer. Anal., 5 (1968), 530-558.

[32] H. Suzuki, Y. Inouo, T. Nishimura, K. Fukutani and K. Suzuki, Unsteady flow in a channel obstructed by a square rod, Int. J. Heat Fluid Fl., 14 (1993), 2-9.

[33] J. C. Tannehill, D. A. Anderson and R. H. Pletcher, Computational Fluid Mechanics and Heat Transfer, Taylor & Francis, New York, 1997.

[34] P. G. Tucker, Computation of Unsteady Internal Flows, Kluwer Academic Publishers, London, 2001.

[35] O. R. Tutty, Pulsatile flow in a constricted channel, J. Biomech. Eng., 114, (1992), 50-54.

[36] P. Wesseling, Principles of Computational Fluid Dynamics, Springer-Verlag, Berlin, Heidelberg, 2001.

[37] D. F. Young and F. Y. Tsai, Flow characteristics in models of arterial stenoses-I. Steady flow, J. Biomech., 6 (1973), 395-410.

[38] G. R. Zendehbudi and M. S. Moayeri, Comparison of physiological and simple pulsatile flows through stenosed arteries, J. Biomech., 32 (1999), 959-965.